Comparison of Monostatic and Bistatic Radar Images

R. J. Burkholder, I. J. Gupta, and J. T. Johnson

The Ohio State University, Department of Electrical Engineering, ElectroScience Laboratory
1320 Kinnear Road, Columbus, OH 43212 USA
Tel: +1 (614) 292-4597; Fax: +1 (614) 292-7297; E-mail: burkhold@ee.eng.ohio-state.edu

Abstract

Relationships between monostatic and bistatic radar images are reviewed and discussed, both from the point of view of identical receiver locations, and from the conventional point of view where the monostatic radar is located at the angular bisector between the bistatic transmitter and receiver. Example images are computed using scattered fields from two three-dimensional (3D) body-of-revolution (BOR) geometries. A Method-of-Moments solution is used to calculate scattered fields so that no scattering interactions are neglected. In the conventional comparison, sample bistatic images show direct-scattering mechanisms similar to those of monostatic images as expected, although significant differences are observed in higher-order scattering effects. With identical receiver locations, the sample bistatic images generated are very different from the monostatic images, and illustrate the practically important fact that geometries designed to minimize monostatic scattering can produce large bistatic returns.

Keywords: Multistatic scattering; radar scattering; radar cross sections; radar imaging; microwave imaging; image processing; boundary integral equations

1. Introduction

Although bistatic radar systems are typically more complex and difficult to implement than monostatic systems [1], the potential of bistatic measurements for detecting low-observable targets motivates continued studies. For example, targets designed to minimize backscatter (monostatic scattering) by reflecting radar energy into other directions might be easily detected by a bistatic system. Radar images offer a unique means for obtaining insight into the scattering behavior of an object if multiple frequency and aspect data are available. Radar images generated from bistatic scattering data have been studied previously in [2], and in many cases found to have properties similar to those generated from monostatic data. However, consideration of the differing scattering effects that can occur for monostatic and bistatic geometries indicates that bistatic and monostatic images may not be necessarily similar, particularly for geometries designed to minimize monostatic cross sections.

In this article, relationships between monostatic and bistatic radar images are reviewed and discussed, using sample images formed from scattering data computed from a body-of-revolution Method-of-Moments algorithm [3-5]. Use of numerical scattering models is advantageous because no scattering effects are explicitly neglected, enabling higher-order interactions to be captured and studied. While the requirement for multiple-frequency and multiple-angle scattering data in image formation for a three-dimensional target makes large-scale computations necessary, currently available methods are sufficiently effective to complete the computations in a reasonable time. Two perfectly conducting targets are considered: a low-observable ogive, and a missile-like cone-cylinder with flared end, with dimensions shown in Figure 1.

The images are generated from two vantage points. In the first case, the bistatic receiver and the monostatic radar are co-located, as shown in Figure 2a. This point of view will be referred to as "receiver-centric;" note that the monostatic transmitter/receiver and the bistatic receiver locations are identical, while the bistatic transmitter has a different location. The angle β is defined as the bistatic angle, and θ_t is the rotation angle of the body-of-

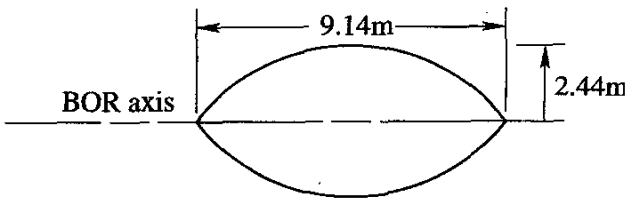

Figure 1a. Three-dimensional BOR geometries: the ogive geometry. The target is a perfect electrical conductor.

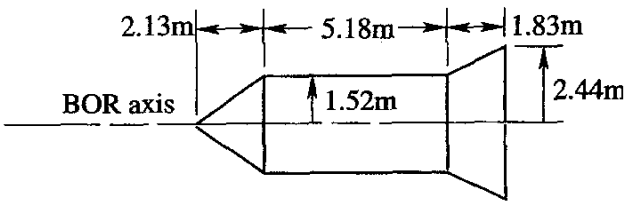

Figure 1b. Three-dimensional BOR geometries: the missile geometry (a cone-cylinder with flared end). The target is a perfect electrical conductor.

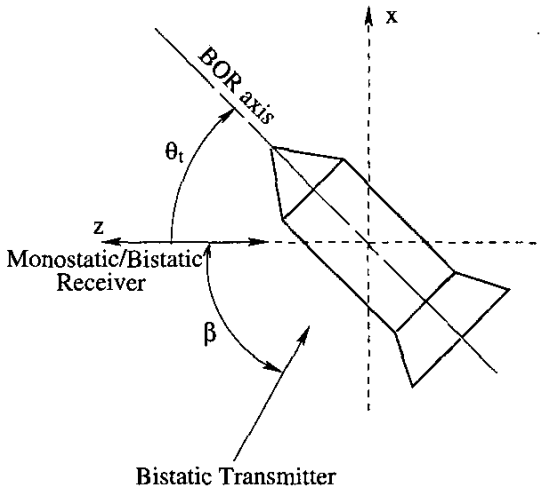

Figure 2a. The coordinate system for receiver-centric images.

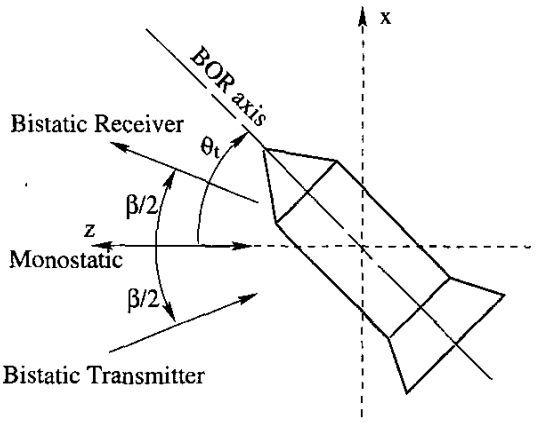

Figure 2b. The coordinate system for conventional images.

revolution (BOR) axis of the target from the positive z axis in the x-z plane. (All images presented in this article are in the x-z plane, for simplicity.) In this case, the monostatic and bistatic radar images can be significantly different, so that geometries designed to minimize monostatic scattering may yield large bistatic returns.

In the past, it has been shown that the monostatic scattering from targets is similar to the bistatic scattering, provided that the monostatic radar is located at the angular bisector of the bistatic receiver and transmitter, and that the monostatic frequency band is multiplied by a factor of $\cos(\beta/2)$ with respect to the bistatic radar frequency band. This is a result of the "monostatic-bistatic equivalence theorem," which is derived by considering only first-order scattering centers [6, 7]. Sample radar images from this vantage point are also illustrated and compared. The coordinate system for these radar images is shown in Figure 2b. We will call these radar images the "conventional images." Sample image results show that conventional bistatic images indeed have an appearance similar to the monostatic images, but the detailed scattering mechanisms can be significantly different. This is especially true for higher-order scattering mechanisms.

The rest of the paper is organized as follows. Section 2 describes the generation of radar images. Scattering computations and single-frequency results are described in Section 3. Section 4 presents sample monostatic, receiver-centric bistatic, and conventional bistatic images for several look angles. A summary of the discussions of the paper is then presented in Section 5.

2. Image Generation

Two-dimensional radar images can be formed from multi-frequency and multi-aspect-angle scattered-field data, for either monostatic or bistatic systems. The imaging method described here is based on an inverse-Fourier-transform-with-back-projection algorithm [8]. In this technique, frequency- and aspect-domain scattered-field data are mapped into image space using the following relationship:

$$I(x,z)=\int_{-\theta_0}^{\theta_0} G\left[\theta,t(x,z,\theta)\right]d\theta, \tag{1}$$

where $I(x,z)$ is the complex-valued image intensity at coordinates x and z, and

$$G[\theta,t]=\int_{f_1}^{f_2}\tilde{E}(f,\theta)e^{-j2\pi ft}df. \tag{2}$$

The "time" function, $t(x,z,\theta)$, in Equations (1) and (2) depends on the imaging geometry, and is described further below. Here, $-\theta_0<\theta<\theta_0$ describes the aspect-angular region over which the transmitter and receiver locations are varied, and $f_1\le f\le f_2$ is the frequency band over which scattered-field data are available. Also, in Equation (2),

$$\tilde{E}(f,\theta)=f\,E(f,\theta)w(f,\theta), \tag{3}$$

where $E(f,\theta)$ is the two-dimensional (complex) scattered-field data; $w(f,\theta)$ is a two-dimensional window function, included to reduce sidelobe levels in the images formed; and the multiplication by f results from an earlier transformation to polar coordinates. In the example images illustrated,

$$w(f,\theta)=w_1(f)w_2(\theta), \tag{4}$$

and $w_1(f)$ and $w_2(f)$ are selected to be Hamming windows.

Equation (2) is a Fourier transform, and, for discretely sampled scattered-field data, can be computed using the fast Fourier transform (FFT). Equation (1) can then be used to obtain the image-domain response, given $t(x,z,\theta)$. Note that use of the FFT implies that t is also discretely sampled; an interpolation algorithm can be used to map discretized values of $t(x,z,\theta)$ to discretely sampled image-space locations.

We can define the radar receiver as located at an angle θ_1, measured clockwise with respect to the positive z axis in the x-z plane (illustrated as zero degrees in Figure 2a). If the radar transmitter is then similarly defined as located at angle θ_2, the excess time delay to travel from the transmitter to a point (x,z) on the target and then to the receiver is

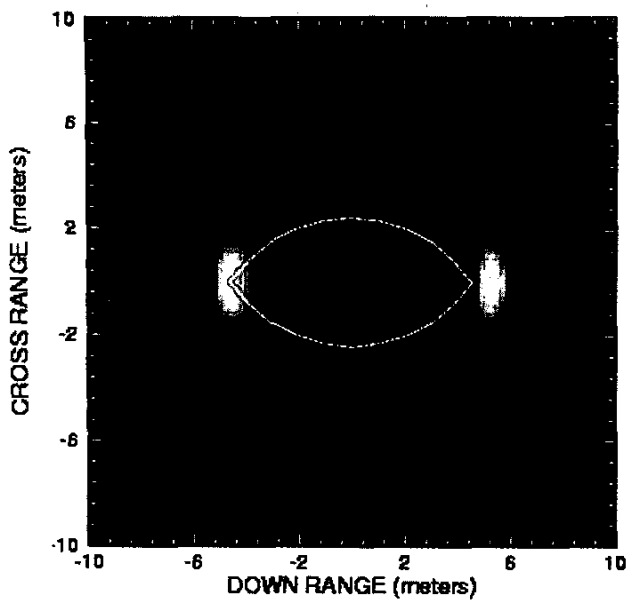

Figure 5a. The receiver-centric monostatic image of the ogive target, $\theta_t = 0°$. The center frequency was 500 MHz, 80% bandwidth.

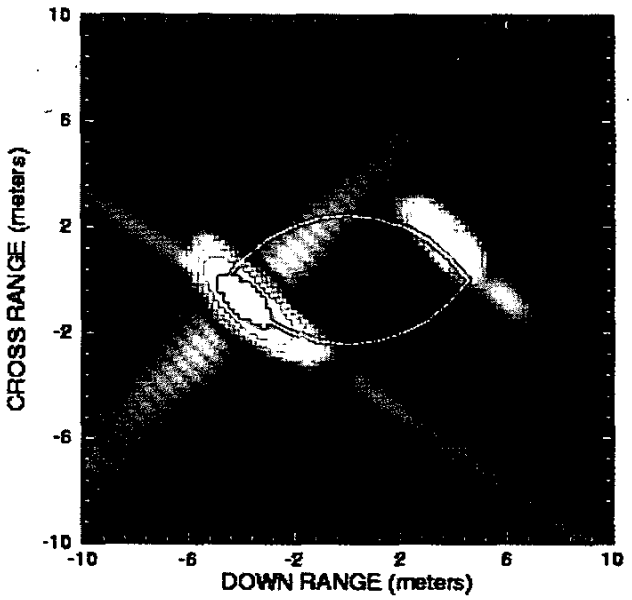

Figure 5b. The receiver-centric bistatic image of the ogive target ($\beta = 90°$), $\theta_t = 0°$. The center frequency was 500 MHz, 80% bandwidth.

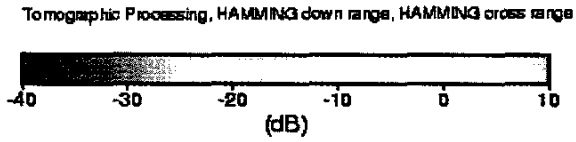

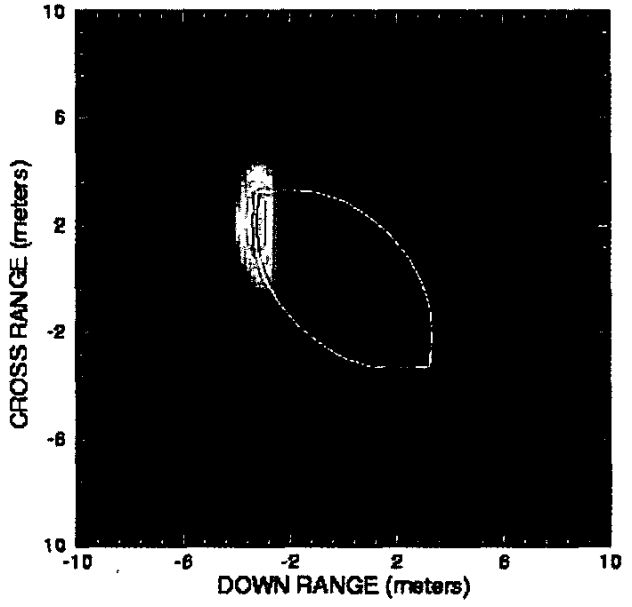

Figure 5c. The receiver-centric monostatic image of the ogive target, $\theta_t = 45°$. The center frequency was 500 MHz, 80% bandwidth.

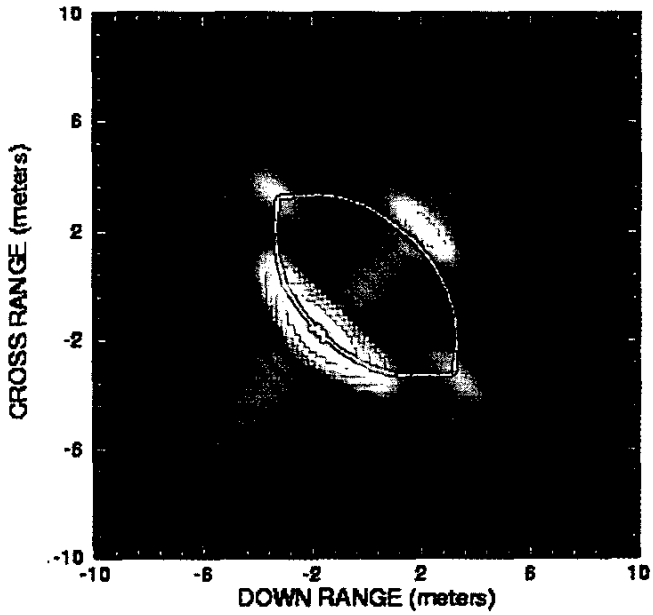

Figure 5d. The receiver-centric bistatic image of the ogive target ($\beta = 90°$), $\theta_t = 45°$. The center frequency was 500 MHz, 80% bandwidth.

$$t(x,z,\theta) = -\frac{1}{c}\left[x(\sin\theta_1 + \sin\theta_2) + z(\cos\theta_1 + \cos\theta_2)\right], \quad (5)$$

where c is the speed of light in free space. The excess time delay is with respect to the time delay to travel from the transmitter to the origin in the x-z plane, and then to the receiver.

In the receiver-centric imaging system (see Figure 2a), $\theta_1 = \theta$, and $\theta_2 = \theta_1 - \beta$, where β is the bistatic angle. The time function is then

$$t(x,z,\theta) = -\frac{1}{c}\left\{x\left[\sin\theta + \sin(\theta-\beta)\right] + z\left[\cos\theta + \cos(\theta-\beta)\right]\right\}. \quad (6)$$

In the conventional imaging geometry (see Figure 2b), $\theta_1 = \theta + \beta/2$ and $\theta_2 = \theta - \beta/2$. The excess-time-delay function from Equation (5) now reduces to

$$t(x,z,\theta) = -\frac{2}{c}\cos(\beta/2)\left[x\sin\theta + z\cos\theta\right]. \quad (7)$$

The geometries of Figures 2a and 2b clearly show that Equations (6) and (7) should be related. The substitution $\gamma = \theta - \beta/2$ into Equation (6) results in a receiver-centric time function identical to Equation (7), but in terms of the angle γ, rather than θ. The receiver-centric bistatic image should thus be identical to the conventional bistatic image, but at a rotated central angle of $\gamma = \theta - \beta/2$. Although this relationship is mathematically simple, it has important practical implications, because bistatic radar images would typically be formed at the receiver location, rather than in the conventional bistatic-image fashion.

For a monostatic radar $\beta = 0°$, so that both Equations (6) and (7) reduce to

$$t_m(x,z,\theta) = -\frac{2}{c}\left[x\sin\theta + z\cos\theta\right], \quad (8)$$

where subscript m is used to indicate the monostatic radar. Equations (7) and (8) are identical with the exception of the factor $\cos(\beta/2)$ in Equation (7). Because the $\cos(\beta/2)$ factor directly multiplies the frequency variable f in the exponential term of the integrand in Equation (2), this can be considered a "frequency scaling factor" compared to the monostatic case. Image comparisons are thus facilitated if the monostatic radar frequency band is taken as $\cos(\beta/2)$ times the bistatic radar frequency band. The imaging processes for the monostatic and "conventional" bistatic images will then produce similar weighting factors for each frequency and angle scattered-field data point in computing the resulting image. The resulting similarity of the images, however, depends not only on the similarity of the time functions in Equations (7) and (8), but also on the similarity of the scattering mechanisms captured by the scattered fields $E(f,\theta)$.

3. Scattered-Field Computations

To demonstrate some sample bistatic and monostatic radar images and their relationships, the *CICERO* body-of-revolution (BOR) Moment-Method code, developed by McDonnell Douglas Research Labs (now Boeing Phantom Works), St. Louis, was used to compute numerical scattering data [5] for the targets illustrated in Figure 1. Three-dimensional objects were created by rotating the generating curves plotted through a full revolution about the BOR axis. The moderate electromagnetic size of the targets considered allowed a direct solution of the Moment-Method matrix equation as implemented in the *CICERO* code, although more-efficient iterative solutions can be applied for larger-size targets. Frequencies ranging from 300 MHz to 700 MHz were included, giving a center frequency of 500 MHz (0.6 m wavelength) and an 80% bandwidth. The total length of the generating curves considered ranged from about 12 to 30 electromagnetic wavelengths. A sampling rate of 15 points per wavelength at the highest frequency was used for all frequencies to insure accuracy, resulting in a maximum of 430 points sampling the generating curve. The BOR formulation allows the total matrix equation to be decoupled into separate

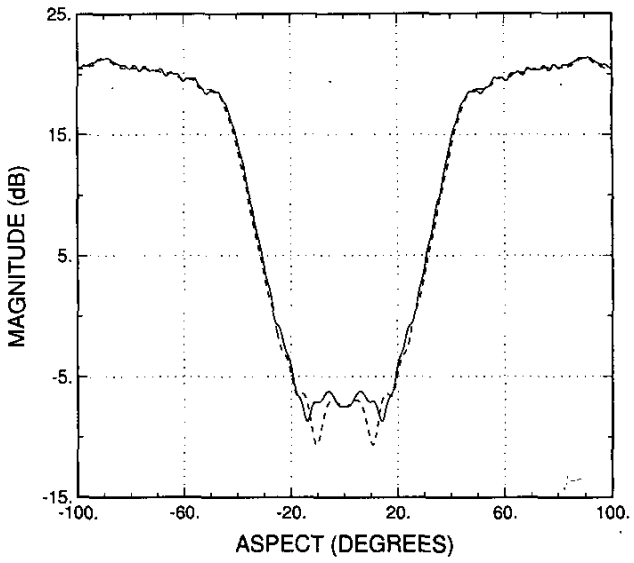

Figure 3a. The monostatic ($\beta = 0°$) RCS aspect-angle pattern of the ogive target at the center frequency of 500 MHz: —— θ polarization, - - - ϕ polarization.

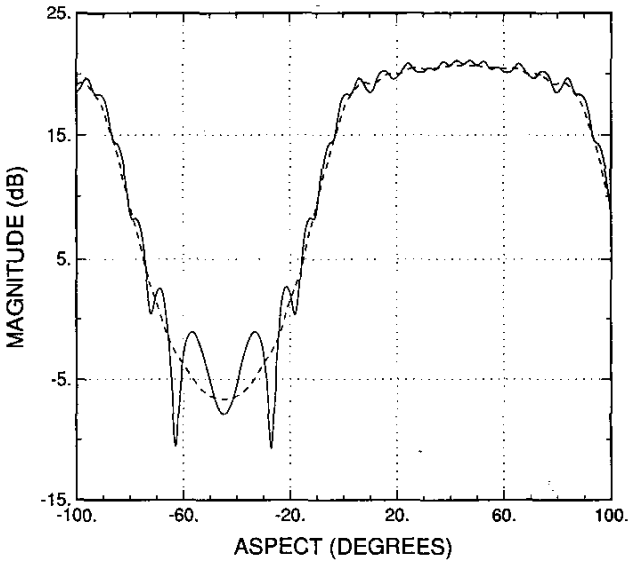

Figure 3b. The bistatic ($\beta = 90°$) RCS aspect-angle pattern of the ogive target at the center frequency of 500 MHz: —— θ polarization, - - - ϕ polarization.

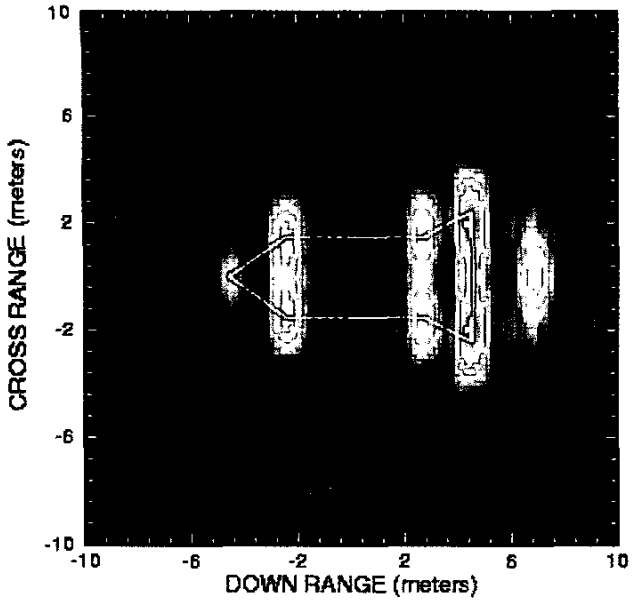

Figure 6a. The receiver-centric monostatic image of the missile target, $\theta_t = 0°$. The center frequency was 500 MHz, 80% bandwidth.

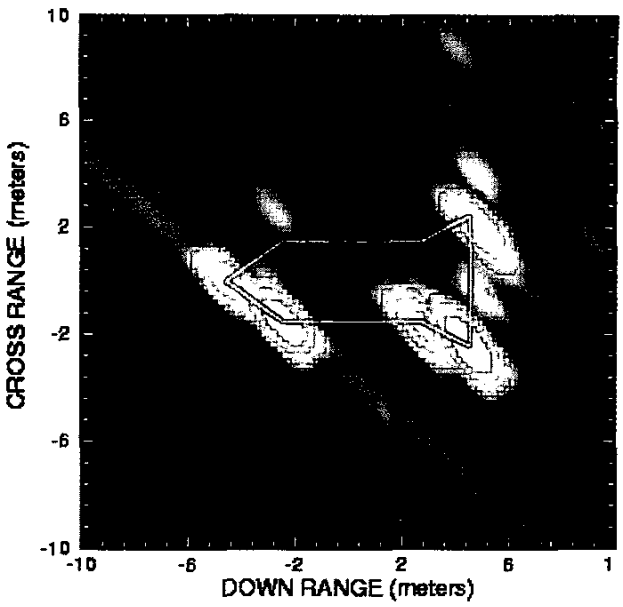

Figure 6b. The receiver-centric bistatic image of the missile target ($\beta = 80°$), $\theta_t = 0°$. The center frequency was 500 MHz, 80% bandwidth.

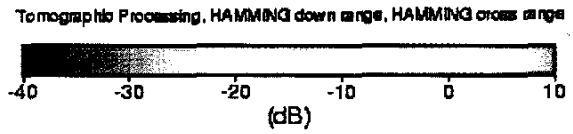

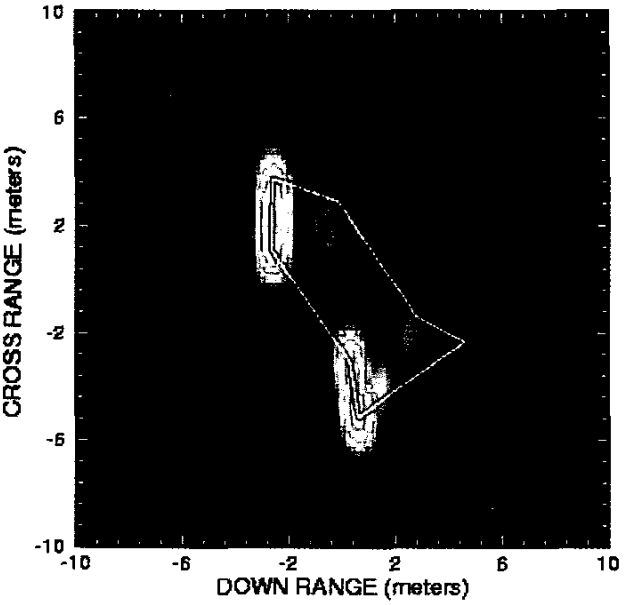

Figure 6c. The receiver-centric monostatic image of the missile target, $\theta_t = 55°$. The center frequency was 500 MHz, 80% bandwidth.

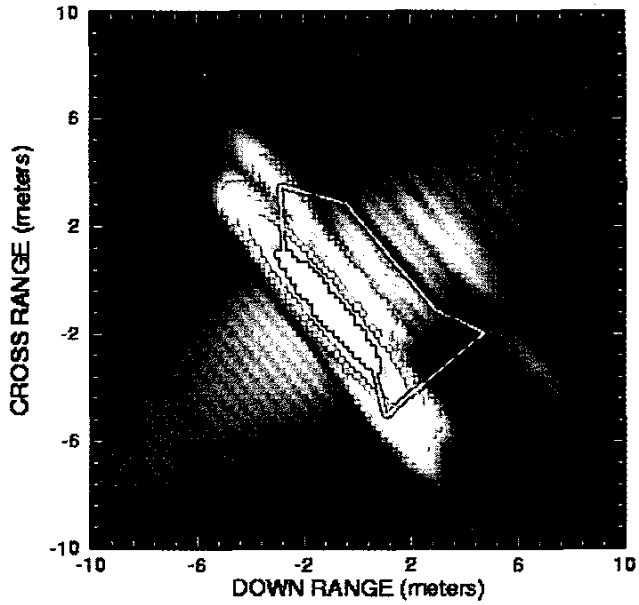

Figure 6d. The receiver-centric bistatic image of the ogive target ($\beta = 80°$), $\theta_t = 55°$. The center frequency was 500 MHz, 80% bandwidth.

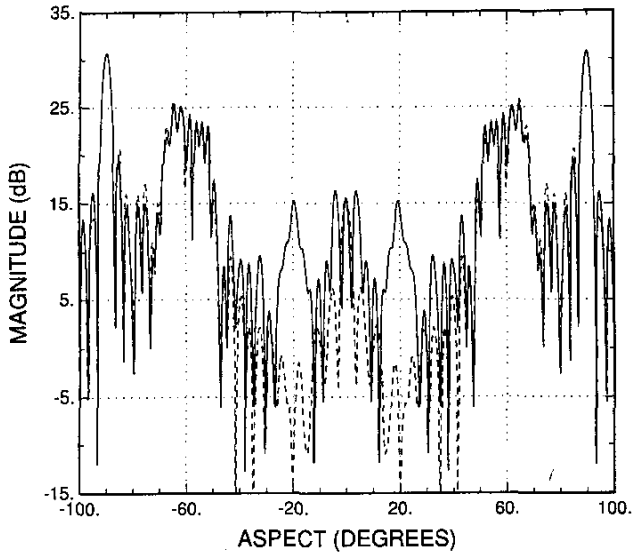

Figure 4a. The monostatic ($\beta = 0°$) RCS aspect-angle pattern of the missile target at the center frequency of 500 MHz: —— θ polarization, - - - ϕ polarization.

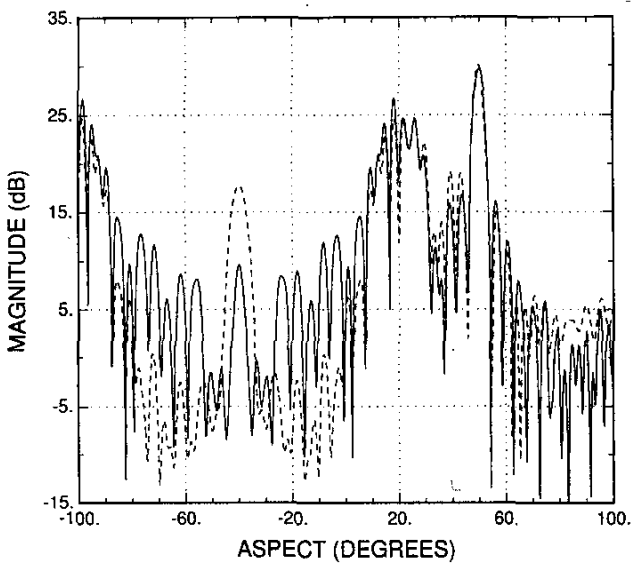

Figure 4b. The bistatic ($\beta = 80°$) RCS aspect-angle pattern of the missile target at the center frequency of 500 MHz: —— θ polarization, - - - ϕ polarization.

matrix equations for each azimuthal harmonic variation; a total of 37 azimuthal harmonics were used at the highest frequency. Calculations were repeated for 80 frequencies in the bandwidth of interest, and the scattering results were computed at radar transmitter angles (aspect angles) ranging from –100° to 100° in steps of 0.25° for both θ and ϕ polarizations in the x-z plane (coordinates shown in Figure 2). The total CPU time required for one set of results at a fixed bistatic angle was approximately 24 hours on a Pentium II 450 MHz processor. Note that the azimuthal symmetry of the geometry results in no cross-polarized scattered-field returns for the cases considered here.

Figure 3 shows the patterns of the computed radar cross section (RCS) as a function of radar transmitter location (aspect-angle) for the ogive target of Figure 1a, at the center frequency of 500 MHz. The receiver-centric coordinate system of Figure 2a was used, and the magnitude of the RCS was plotted as a function of aspect angle. The bistatic angle was $\beta = 90°$ in Figure 3b, so the bistatic patterns should show similar dominant features compared with the monostatic patterns, but shifted left by $45°(\beta/2)$. As expected, the RCS is very low in the nose-on region, where the scattering is dominated by tip diffraction, and is high in the regions dominated by specular reflection. For bistatic scattering, there appears to be interference between two equal scattering mechanisms in the nose-on region of the bistatic θ polarization case. The radar images should identify these mechanisms.

Figure 4 shows the corresponding RCS data for the missile target of Figure 1b. The bistatic angle for Figure 4b is $\beta = 80°$, so the bistatic patterns were expected to show similar dominant features compared with the monostatic patterns shifted left by 40°. Both plots show the strong broadside specular return at ±90° for monostatic and at 50° for bistatic. The specular returns from the sides of the cone and flare sections were expected to be at 55° and 64°, respectively, in the monostatic plot, and at 15° and 24° for bistatic. They are seen blurred together in the 50° - 70° range for monostatic and in the 10° - 30° range for bistatic. In the near nose-on region, it is interesting to note that there are significant differences between the monostatic and bistatic cases. The monostatic patterns show more-complex scattering in the nose-on region, probably due to the ring caustics associated with the trailing edge of the flare end and the junctions between sections. The images will also help clarify these mechanisms.

To generate the radar images for a target rotated to angle θ_t in the x-z plane, the radar central-angle locations were fixed as shown in Figure 2. Images were formed by rotating the radar transmitter and receiver locations through a ±10° span about the central-angle locations, while maintaining a fixed bistatic angle β between the transmitter and receiver. For simplicity, rotations of the target or radar systems out of the x-z plane were not considered. Because the scattered fields for θ and ϕ polarization typically are somewhat similar, the polarization of the incident and scattered fields in the images was limited to the x-z plane (θ polarization). An 80% bandwidth and a ±10° aspect region at 500 MHz center frequency, with 5 MHz and 0.25° step sizes, led to $0.375/\cos(\beta/2)$ meters down-range and $0.86/\cos(\beta/2)$ meters cross-range resolution [2]. The "frequency-scaling" factor, derived in Section 2, results in down-range and cross-range resolutions that degrade with the bistatic angle when compared to the same bandwidth monostatic image. The corresponding down-range and cross-range unambiguous intervals were $30/\cos(\beta/2)$ meters and $68.75/\cos(\beta/2)$ meters, respectively. These parameters were sufficient to allow reasonable images to be constructed.

4. Sample Images

4.1 Receiver-Centric Radar Images

The ogive-shaped geometry of Figure 1a is considered first. This target has a low monostatic radar cross section for aspect angles close to nose-on. Figures 5a and 5b, respectively, show the monostatic and bistatic images of the ogive for $\theta_t = 0°$ from the

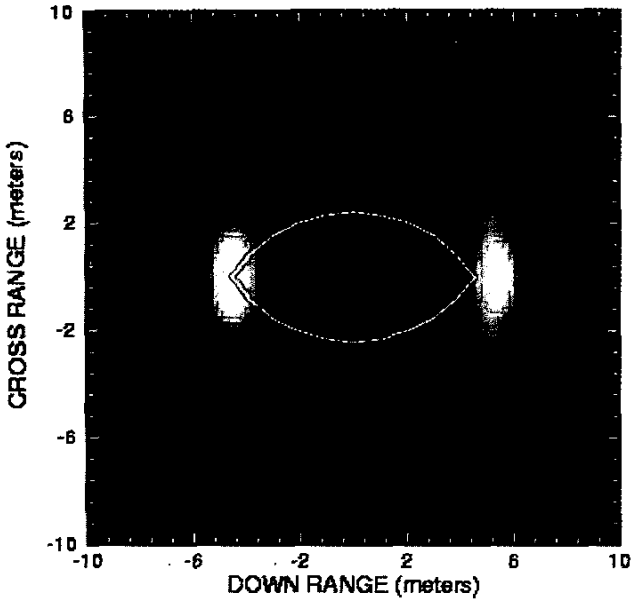

Figure 7a. The conventional monostatic image of the ogive target, $\theta_t = 0°$. The center frequency was 354 MHz, 80% bandwidth.

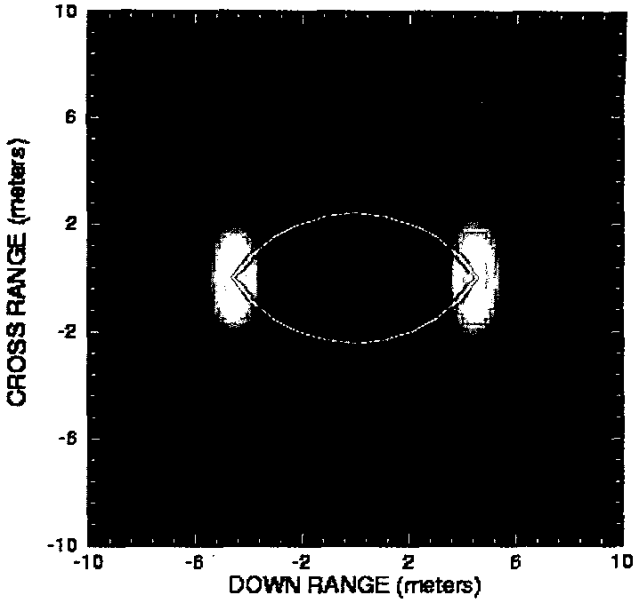

Figure 7b. The conventional bistatic image of the ogive target ($\beta = 90°$), $\theta_t = 0°$. The center frequency was 500 MHz, 80% bandwidth.

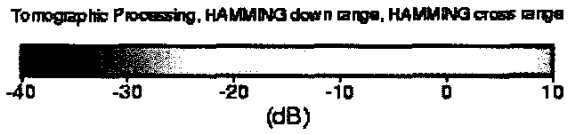

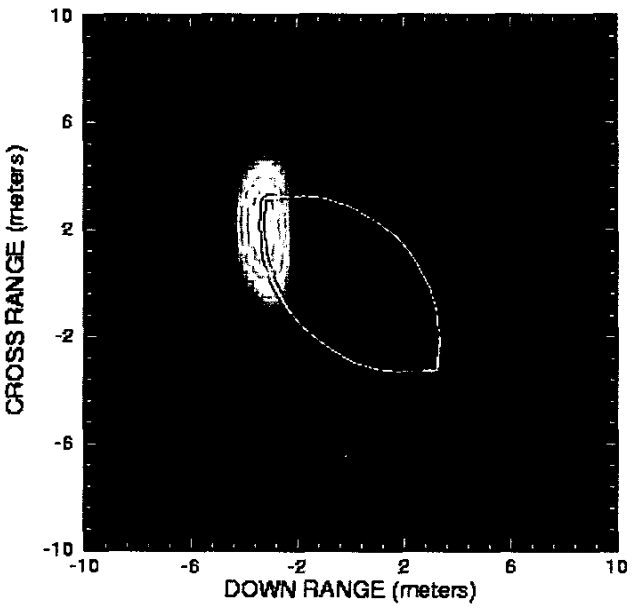

Figure 7c. The conventional monostatic image of the ogive target, $\theta_t = 45°$. The center frequency was 354 MHz, 80% bandwidth.

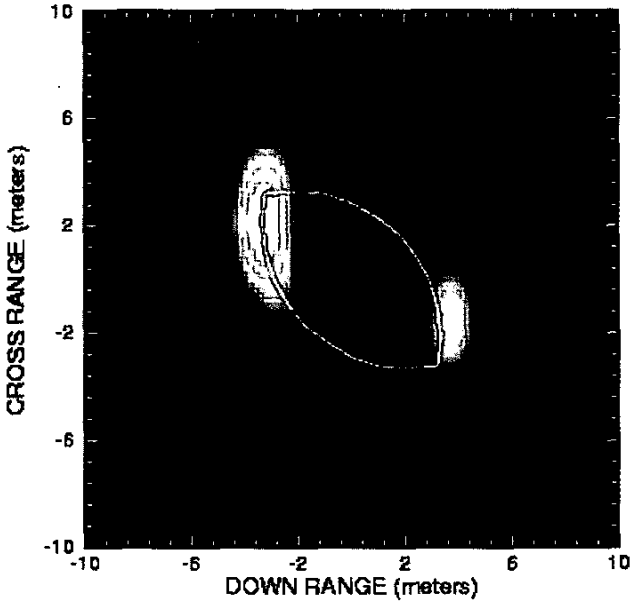

Figure 7d. The conventional bistatic image of the ogive target ($\beta = 90°$), $\theta_t = 45°$. The center frequency was 500 MHz, 80% bandwidth.

point of view of the receiver (receiver-centric). A bistatic angle of $\beta = 90°$ was used. As expected, the monostatic image shows relatively weak scattering from the tips of the ogive, whereas the bistatic image shows a very strong scattering center due to a near-specular reflection. Clearly, the images are very different, but they illustrate the importance of considering bistatic scattering mechanisms from the point of view of the receiver when analyzing low-observable targets. Figures 5c and 5d show the receiver-centric images for $\theta_t = 45°$. It should be noted that the color scale is shifted up by 10 dB in Figures 5c and 5d with respect to Figures 5a and 5b. Again, the monostatic and bistatic images are quite different in that the specular-scattering mechanisms dominating the two images are entirely different. The bistatic image also contains some higher-order mechanisms that are missing in the monostatic image.

The simple cone-cylinder target with flared end, depicted in Figure 1b, is considered next, so that several distinct scattering mechanisms can be observed. The bistatic angle was $\beta = 80°$. The missile target will clearly have monostatic specular-like returns from the cylinder portion of the object when $\theta_t = 90°$, and from the flat portions of the cone and flared regions when θ_t is approximately 55° and 64°, respectively, as was seen in Figure 4. Diffraction mechanisms should be expected from the cone tip and the edges at the cone-cylinder and cylinder-flare junctions and the flared end. These effects will assist in interpreting image responses in the following results.

Figure 6 shows the receiver-centric radar images of the missile target. As with the ogive, the bistatic images are significantly different from the monostatic images. The nose-on ($\theta_t = 0°$) monostatic case shows strong, symmetric scattering from the ring caustics formed by the junctions between the cone, cylinder, and flare sections, while the corresponding bistatic image is clearly weighted toward the direction of the incident plane wave and does not show the ring caustics. In the $\theta_t = 55°$ case, the monostatic image shows strong near-specular scattering from the cone and flare sections, whereas the bistatic image shows near-specular scattering from the cylinder section. As mentioned before, the purpose of studying these receiver-centric images is to accentuate the very different scattering mechanisms observed by monostatic and bistatic radars in practice.

4.2 Conventional Radar Images

As shown in Section 2, monostatic and bistatic images of a target should be similar, provided that the monostatic receiver is located along the angular bisector of the bistatic transmitter and receiver, and that the frequency band for the monostatic radar is multiplied by a factor of $\cos(\beta/2)$ (i.e., $\cos(\beta/2)300 < f < \cos(\beta/2)700$ MHz). Monostatic scattered-field data for the sample targets was recalculated in this band to allow image comparisons. Conventional radar images for the ogive are shown in Figure 7. The monostatic and bistatic radar images appear very similar; however, some of the scattering mechanisms contributing to the radar images are different. For example, in the $\theta_t = 0°$ monostatic case, the trailing-edge scattering center is displaced from the body because it is in the shadow of the incident field, unlike the bistatic case, where the trailing tip is illuminated by the incident field. The $\theta_t = 45°$ bistatic case shows a stronger scattering mechanism associated with the trailing tip than in the monostatic image, and it is also displaced slightly from the physical boundary. It is interesting to note that the two scattering centers in Figure 7b are of comparable magnitude, which explains the strong interference observed in the pattern of Figure 3b in the nose-on region.

Figure 8 shows the conventional radar images of the missile target. In the nose-on case ($\theta_t = 0°$), the first-order scattering from the tip and the ring junction between the cone and cylinder sections is very similar in the monostatic and bistatic images, but the scattering from the flare region is quite different. The monostatic radar sees strong ring caustics associated with the junction between the cylinder and flare sections, and the trailing edge of the flare. This explains the behavior of the monostatic scattering pattern of Figure 4a in the near-nose-on region. These rings are partially shadowed in the bistatic image, and so are less distinct. Both the monostatic and conventional bistatic images also show a second-order scattering mechanism off the target boundary, due to an edge interaction across the flared end, but the bistatic image shows several additional higher-order scattering mechanisms clustered around the flare section. (Higher-order scattering mechanisms are evidenced by scattering centers lying off the target's surface.) The $\theta_t = 55°$ case shows very similar near-specular scattering from the cone and flare sections. It is interesting to note that the bistatic image shows a scattering center on the rightmost edge of the flare end that is absent from the monostatic image. This is likely because the rightmost edge is shadowed from the incident field in the monostatic case.

5. Conclusions

The discussions of this paper have reviewed and illustrated some of the basic features of bistatic radar images. Bistatic images generally produce direct-scattering mechanisms (such as specular-like or single diffraction) similar to those of monostatic images when compared in the conventional image sense, but significant differences can be observed in higher-order scattering effects. Capturing these differences requires accurate scattering models, to insure that no mechanisms are neglected. The fact that bistatic images formed from the point of view of the receiver are similar to monostatic images at a different central observation angle is important in practice for understanding and interpreting the imaging performance of bistatic systems.

6. Acknowledgment

The authors would like to thank Mr. John Putnam of Boeing Phantom Works, St. Louis, for providing the *CICERO* code and technical support.

7. References

1. N. J. Willis, "Bistatic Radar," in M. Skolnik (ed.), *Radar Handbook, Second edition*, New York, McGraw-Hill, 1990, Chapter 25.

2. D. L. Mensa, *High Resolution Radar Cross-Section Imaging*, Norwood, MA, Artech House, 1991.

3. M. G. Andreasen, "Scattering from Bodies of Revolution," *IEEE Transactions on Antennas and Propagation*, **AP-13**, 1965, pp. 303-310.

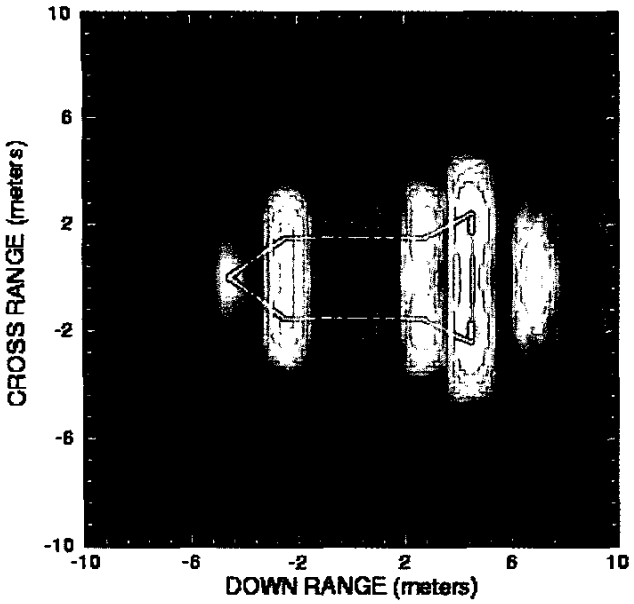

Figure 8a. The conventional monostatic image of the missile target, $\theta_t = 0°$. The center frequency was 354 MHz, 80% bandwidth.

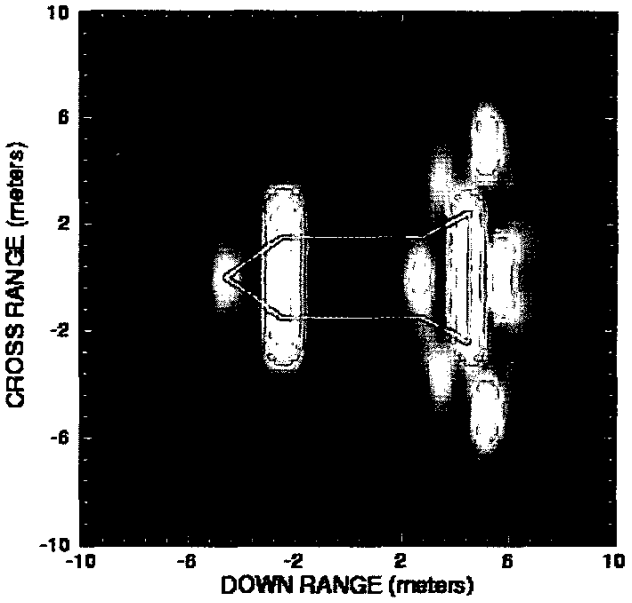

Figure 8b. The conventional bistatic image of the missile target ($\beta = 80°$), $\theta_t = 0°$. The center frequency was 500 MHz, 80% bandwidth.

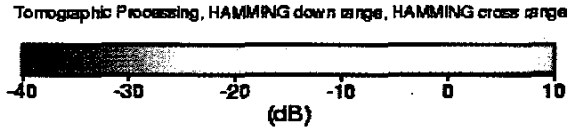

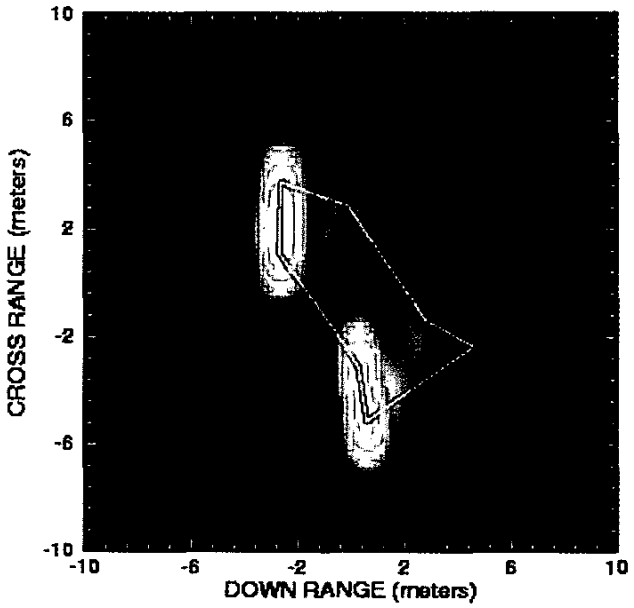

Figure 8c. The conventional monostatic image of the missile target, $\theta_t = 55°$. The center frequency was 354 MHz, 80% bandwidth.

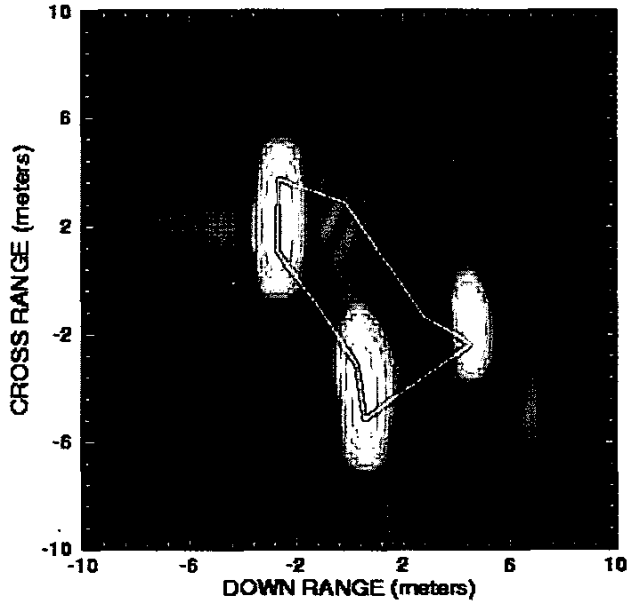

Figure 8d. The conventional bistatic image of the missile target ($\beta = 80°$), $\theta_t = 55°$. The center frequency was 500 MHz, 80% bandwidth.

4. J. R. Mautz, and R. F. Harrington, "Radiation and Scattering from Bodies of Revolution," *Appl. Sci. Res.*, **20**, 1969, pp. 405-435.

5. L. N. Medgyesi-Mitschang, and J. M. Putnam, "Electromagnetic Scattering from Axially Inhomogeneous Bodies of Revolution," *IEEE Transactions on Antennas and Propagation*, **AP-32**, 1984, pp. 797-806.

6. J. W. Crispin, and K. M. Siegel, *Methods of Radar Cross Section Analysis*, Ne York, Academic Press, 1968.

7. G. T. Ruck, D. E. Barrick, W. D. Stuart, and C. K. Krichbaum, *Radar Cross Section Handbook*, New York, Plenum Press, 1970.

8. I. J. Gupta, "Computer Code for Imaging, Editing, and Reconstruction of Radar Data: RDIEAR," Tech. Report 727723-7, The Ohio State University ElectroScience Laboratory, 1995.

Introducing the Feature Article Authors

Robert J. Burkholder received the BS, MS, and PhD degrees in Electrical Engineering from The Ohio State University, Columbus, in 1984, 1985, and 1989, respectively.

From 1989 to the present, Dr. Burkholder has been with The Ohio State University ElectroScience Laboratory, Department of Electrical Engineering, where he currently has the titles of Research Scientist and Adjunct Associate Professor. His research specialties are high-frequency asymptotic techniques and their hybrid combination with numerical techniques for solving large-scale electromagnetic radiation and scattering problems. He has contributed extensively to the EM analysis of large cavities, such as jet inlets/exhausts, and on the more general problem of EM radiation, propagation, and scattering in realistically complex environments.

Dr. Burkholder is a member of USNC/URSI Commission B, and a member of the Applied Computational Electromagnetics Society (ACES). He received the Ohio State University College of Engineering Lumley Research Award for 1996 and 2002.

Dr. **Inder J. Gupta** received the BSc degree in Electronics Engineering from Panjab University, India, in 1975, the MTech degree in Electrical Engineering from the Indian Institute of Technology, Kanpur, India in 1977, and the PhD degree in Electrical Engineering from The Ohio State University, Columbus, Ohio in 1982.

Since 1979, he has been working at the Ohio State University ElectroScience Laboratory where he presently is a Senior Research Scientist. His previous work experience includes Research Engineer at IIT Kanpur, India, and Graduate Research Associate at University of Tennessee Space Institute. He has done extensive research on Adaptive Antenna Systems and Compact Range Measurement Systems, and has written several research articles in these areas. His current research interests include adaptive antenna arrays, AI techniques, electromagnetic scattering, compact range technology, radar imaging, and target recognition.

Dr. Gupta was the President of Antenna Measurement Techniques Association during 1997. He received IEEE Antennas and Propagation Society's H. A. Wheeler Applications Prize Paper Award in 1991. He was also the recipient of the Ohio State University College of Engineering Lumley Research Award for 1991 and 1998.

Joel T. Johnson received the Bachelor of Electrical Engineering degree from the Georgia Institute of Technology in 1991, and the SM and PhD degrees from the Massachusetts Institute of Technology in 1993 and 1996, respectively.

Dr. Johnson is currently an Associate Professor in the Department of Electrical Engineering and ElectroScience Laboratory of The Ohio State University. His research interests are in the areas of microwave remote sensing, propagation, and electromagnetic wave theory.

Dr. Johnson is a member of USNC/URSI Commissions B and F, and a member of Tau Beta Pi, Eta Kappa Nu, and Phi Kappa Phi. He received the 1993 Best Paper Award from the IEEE Geoscience and Remote Sensing Society, was named an Office of Naval Research Young Investigator, a National Science Foundation Career awardee, and a PECASE award recipient in 1997. He was recognized by the US National Committee of URSI as a Booker Fellow in 2002.